actuators

MDPI

Article

Investigation on the Reduced-Order Model for the Hydrofoil of the Blended-Wing-Body Underwater Glider Flow Control with Steady-Stream Suction and Jets Based on the POD Method

Huan Wang, Xiaoxu Du * and Yuli Hu

School of Marine Science and Technology, Northwestern Polytechnical University, Xi'an 710072, China; wanghuan@nwpu.edu.cn (H.W.); zx670821@nwpu.edu.cn (Y.H.)
* Correspondence: nwpudu@163.com

Abstract: The rapid acquisition of flow field characterization information is crucial for closed-loop active flow control. The proper orthogonal decomposition (POD) method is a widely used flow field downscaling modeling method to obtain flow characteristics effectively. Based on the POD method, a flow field reduced-order model (ROM) is constructed in this paper for the flow field control of a hydrofoil of a blended-wing-body underwater glider (BWB-UG) with stabilized suction and blowing forces. Compared with the computational fluid dynamics (CFD) simulation, the computational time required to predict the target flow field using the established POD-ROM is only about 0.1 s, which is significantly less than the CFD simulation time. The average relative error of the predicted surface pressure is not more than 6.9%. These results confirm the accuracy and efficiency of the POD-ROM in reconstructing flow characteristics. The timeliness problem of fast flow field prediction in BWB-UG active flow control is solved by establishing a fast prediction model in an innovative way.

Keywords: proper orthogonal decomposition; active flow control; reduced-order model

Citation: Wang, H.; Du, X.; Hu, Y. Investigation on the Reduced-Order Model for the Hydrofoil of the Blended-Wing-Body Underwater Glider Flow Control with Steady-Stream Suction and Jets Based on the POD Method. *Actuators* **2024**, *13*, 194. https://doi.org/10.3390/act13060194

Academic Editor: Luigi de Luca

Received: 26 March 2024
Revised: 18 May 2024
Accepted: 18 May 2024
Published: 21 May 2024

1. Introduction

The blended-wing-body underwater glider (BWB-UG) is a new type of underwater glider with a flying wing layout. Compared with traditional underwater vehicles, BWB-UGs have advantages such as long range, long operation time, and good economic performance [1]. Various types of underwater gliders have been widely used in fields such as marine resource development and environmental monitoring. The lift–drag ratio is an important factor to measure the performance of underwater gliders. The larger the lift–drag ratio, the greater the range under a single gliding cycle and the higher the gliding efficiency. Therefore, increasing the lift–drag ratio is the key to improving the overall performance of gliders. By optimizing the shape of the underwater glider, the lift–drag ratio can be improved to some extent, but relying solely on shape optimization is limited by flow separation and reduced internal space, which severely limits the detection capability of underwater gliders [2].

Active flow control (AFC) technology is an important method for improving the lift–drag performance of underwater gliders. It can be used to improve the flow field and suppress noise by applying appropriate local perturbations to the flow environment, coupled with the original flow field, to achieve local or global flow changes with low energy consumption [3]. Common AFC techniques include blowing and suction [4], synthetic jets [5], plasma [6], electromagnetic [7], micro-electro-mechanical systems, and smart materials such as adaptive structures [8]. These methods are used in the design and aerodynamic layout of aircraft to significantly improve the maneuverability and flight efficiency. For example, constant-jet active flow control technology is widely used in aeronautical applications such as increasing the lift–drag ratio of wind turbines, controlling the flow separation of axial-pressure gases in aircraft engines, and improving the aerodynamic

performance of aircraft wings [9–11]. Based on the published research results, it can be concluded that blowing and suction, synthetic jets, and electromagnetic jets can all be used in the AFC of the BWB-UG. Although plasma, micro-electro-mechanical systems, etc., have not been used in the field of underwater vehicles, they can provide new ideas for further research. Currently, research on AFC techniques is dominated by passive and open-loop active flow control, while the investigation on closed-loop active flow control is still in its infancy. In previous research, a detailed analysis of the flow field and hydrodynamic characteristics of the BWB-UG equipped with steady blowing suction active flow control has been conducted [12]. On this basis, a reduced-order model (ROM) investigation for the hydrofoil of the BWB-UG flow control with steady-stream suction and jets based on the POD method was carried out in this paper. The key to achieving closed-loop AFC is to solve the problem of real-time calculation, and the establishment of a reduced-order model of the flow field is one of the effective methods. That is, a low-order flow model is built to simulate the original high-order model. Solving the low-order model can significantly reduce the dimensionality of the computation, the amount of computation, and the computation time [13]. As a result, rapid acquisition of flow field characteristic information is achieved, so that the control strategy can be dynamically adjusted to achieve the optimum control effect.

The proper orthogonal decomposition (POD) method has become one of the most popular and widely used order reduction methods (ROMs) due to its ability to efficiently reduce the order of a nonlinear system with very small error [14]. The POD method provides the most optimal orthogonal basis, so that the projection of the sample data onto these standard orthogonal basis decreases rapidly. By intercepting the first few orders of modes with larger projections (containing higher energies), an approximate description of higher-order data with fewer modal expansions can be achieved. That is, by extracting the main feature information of the flow field to establish a ROM, the information in the flow field can be reconstructed [15].

Since Lumely [16] applied the POD method to the study of turbulence, scholars have used the POD method for flow field analysis and conducted a large number of studies. Kidambi et al. [17] studied a nonlinear control method based on POD, which effectively achieved the asymptotic adjustment of fluid velocity in a specified spatial domain. Wang et al. [18] developed a low-dimensional ordinary differential model for the control of static N-S equations based on the POD method. Min et al. [19] conducted a modal analysis of parallel double cylinders using two data-driven methods: appropriate orthogonal decomposition (POD) and dynamic mode decomposition (DMD). Sun et al. [20] proposed a ROM of wind turbine blade flow fields, coupling an air–fluid reduced-order model with wind turbine blades for fluid–solid coupling calculations, and it was shown that the ROM has good accuracy and validity. Combining the raw data from wind tunnel experiments, Wang et al. [21] applied POD combined with the interpolation method to predict the wind pressure field. A nonlinear Galerkin method using POD for the low-dimensional modeling of complex hydrodynamic systems was proposed by Kang et al. [22].

It has been shown that AFC technology has excellent potential for application in improving the performance of underwater gliders. However, from the public research literature, some preliminary research results have been achieved on the technical application of open-loop AFC for BWB-UGs, there are relatively few studies on ROMs of the flow field for closed-loop AFC, most of public papers are applied in aerospace and astronautics, and there are very few studies applied in underwater gliders. Therefore, the investigation of the reduced-order model for the hydrofoil of the BWB-UG flow control based on the POD method is of great theoretical significance and application value for solving the important problems in the closed-loop AFC of BWB-UGs.

In this paper, the hydrofoil of a BWB-UG under active flow control is investigated. Section 2 introduces the physical model, the numerical computational model, and POD method. Section 3 deals with the discussion and analysis of the results. In this section, the flow field information both before and after the application of AFC is sampled, the

ROM is calculated based on simulated data and using the POD method, then the flow field prediction is achieved using interpolated predicted modal coefficients. After comparing the results with the CFD simulations, conclusions are drawn in Section 4.

2. Model and Method

2.1. Physical Model

The hydrofoil model selected for this paper comes from the BWB-UG, which is a correction of the NACA0012 standard hydrofoil as shown in Figure 1. It has a chord length of 100 mm and a maximum thickness of 0.12 c at 0.3 c from the leading edge of the hydrofoil, which is slightly thicker near the leading and trailing edges compared to the NACA0012. The effects of parameters such as the angle of attack of the incoming flow (α), the constant suction/jet angle ($\theta_{suction}/\theta_{jet}$), and the velocity ($V_{suction}/V_{jet}$) are mainly considered in the active control of the hydrofoil flow field. The constant suction position is located at 0.7 c from the leading edge of the hydrofoil on the upper surface, with a suction opening width h. The jet position is set at 0.5 c from the leading edge of the hydrofoil on the lower surface, with a jet opening width h. As shown in Figure 2, h is defined as the width of the jet opening along the direction of the chord length with a magnitude of 0.01 c.

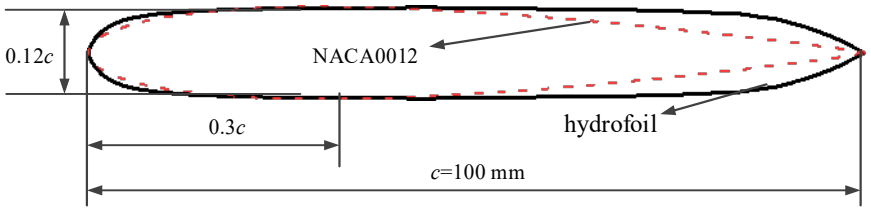

Figure 1. Hydrofoil profile geometry model.

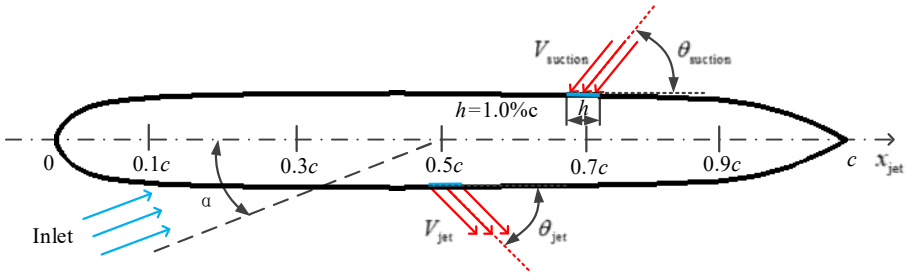

Figure 2. Hydrofoil flow control with steady-stream suction and jets.

2.2. Numerical Sampling Method

In this paper, the flow field in the hydrofoil of a BWB-UG is investigated based on the two-dimensional Reynolds-averaged Navier–Stokes equations (RANS) [23], the fluid medium is incompressible seawater, and the governing equations are as follows:

$$\frac{\partial \rho}{\partial x} + \frac{\partial \rho}{\partial y} = 0 \tag{1}$$

$$\rho\left(\frac{\partial \overline{u}}{\partial t} + \overline{u}\frac{\partial \overline{u}}{\partial x} + \overline{v}\frac{\partial \overline{u}}{\partial y} + \overline{w}\frac{\partial \overline{u}}{\partial z}\right) = \mu\left(\frac{\partial^2 \overline{u}}{\partial x^2} + \frac{\partial^2 \overline{u}}{\partial y^2}\right) + \left(\frac{\partial\left(-\rho\overline{u'u'}\right)}{\partial x} + \frac{\partial\left(-\rho\overline{u'v'}\right)}{\partial y}\right) - \frac{\partial p}{\partial x} \tag{2}$$

$$\rho\left(\frac{\partial \overline{v}}{\partial t} + \overline{u}\frac{\partial \overline{v}}{\partial x} + \overline{v}\frac{\partial \overline{v}}{\partial y}\right) = \mu\left(\frac{\partial^2 \overline{v}}{\partial x^2} + \frac{\partial^2 \overline{v}}{\partial y^2}\right) + \left(\frac{\partial\left(-\rho\overline{v'u'}\right)}{\partial x} + \frac{\partial\left(-\rho\overline{v'v'}\right)}{\partial y}\right) - \frac{\partial p}{\partial y} \tag{3}$$

where p is the pressure; μ is the dynamic viscosity coefficient; $\overline{u}$, $\overline{v}$, and $\overline{w}$ are the time-averaged velocity components of the fluid in the x, y, z directions; and u', v', w' are the velocity fluctuations of the fluid in the x, y, z directions.

A semicircular and rectangular plane region is adopted as the computational domain, considering hydrofoil flow characteristics with AFC. The semicircular section has a radius of 10 c, with the center of the circle located at the trailing edge of the hydrofoil, and the rectangular section is 20 c × 15 c. The 2D structured grid has been meshed. The inlet boundary is set to the inlet velocity, the specified velocity $V_{inlet} = 0.514$ m/s, and the velocity direction is determined by the angle of attack. The jet inlet boundary is also set as a velocity inlet, with the velocity magnitude determined by V_{jet} and $V_{suction}$, and the velocity direction is determined by $\theta_{suction}$ and θ_{jet}. The outlet boundary is set as a pressure outlet, the hydrofoil surface is a non-slip surface, and the specific computational setup and mesh setup are shown in Figures 3 and 4. The enhanced wall treatment is used. The first grid height of the boundary layer is 5×10^{-5} m, the number of boundary layers is 15, and the thickness of the boundary layer is 1.8×10^{-3} m. The gird parameters are set to ensure that the maximum $y^+ = 0.96$ for the hydrofoil surface.

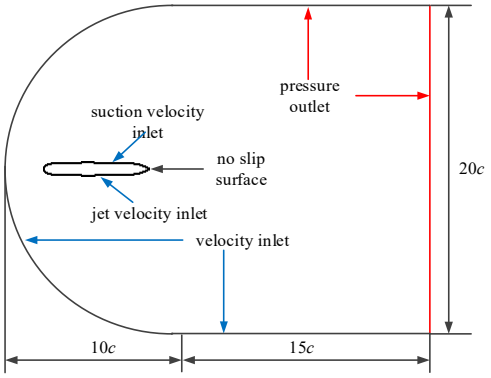

Figure 3. Computational domain and boundary conditions.

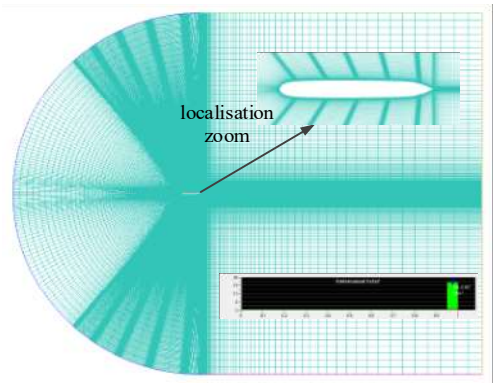

Figure 4. Computational domain meshing.

The SIMPLEC algorithm coupled with pressure and velocity in ANSYS FLUENT was chosen to solve the equations for numerical calculations. The k-ω SST is chosen as the turbulence model, and the transport equations of k and w are expressed as the following [24]:

$$\begin{cases} \frac{\partial(\rho k)}{\partial t} + \frac{\partial(\rho \overline{U}_i k)}{\partial x_i} = P_k + D_k + \frac{\partial}{\partial x_i}\left[(\mu + \sigma_k \mu_t)\frac{\partial k}{\partial x_i}\right] \\ \frac{\partial(\rho \omega)}{\partial t} + \frac{\partial(\rho \overline{U}_i \omega)}{\partial x_i} = P_\omega + D_\omega + \frac{\partial}{\partial x_i}\left[(\mu + \sigma_\omega \mu_t)\frac{\partial \omega}{\partial x_i}\right] \end{cases} \quad (4)$$

where $\overline{U}_i$ is the component of the flow velocity along the direction x_i $(i = 1, 2, 3)$; μ is the dynamic viscous coefficient of the fluid; σ_k and σ_ω are the modeling coefficients; P_k and P_ω are the generating terms; D_k and D_ω are the dissipative terms; and μ_t is the turbulent viscous coefficient.

The spatial discretization of the variables is chosen to be in the second-order upwind format, the finite volume method is chosen as the solver, and the residual convergence criterion is set to 10^6. The specific fluid medium is set to be incompressible seawater at 20° Celsius with a density of $\rho = 1.024 \times 10^{-3}$ kg/m^3, the dynamic viscosity coefficient is set to be a constant, $\mu = 1.0797 \times 10^{-3}$kg/(ms^{-1}), and the Reynolds number based on the hydrofoil chord length is $Re\_c = 5 \times 10^5$. The calculations are performed using the pressure solver in ANSYS FLUENT.

In order to ensure that the flow field calculations have sufficient computational accuracy and efficiency, grid independence validation is carried out to select the appropriate number of meshes. Constant suction active flow control is imposed on the hydrofoil profile by constantly adjusting the global mesh number. The incoming flow velocity is 0.514 m/s. The suction velocity coefficient is 1. The suction deflection angle is 30°. The angle of attack is 2°/6°/10°. The values of lift coefficients for different mesh sizes are shown in the Table 1.

Table 1. Grid independence validation.

Mesh Number	Lift Coefficient		
	AOA = 2°	AOA = 6°	AOA = 10°
76000	0.2683	0.5895	0.5384
105000	0.2639	0.5886	0.5378
135000	0.2612	0.5861	0.5352
164000	0.2612	0.586	0.535

2.3. POD Method

The core idea of the POD method is to find the optimal standard orthogonal basis functions in the mean-square sense from a set of time-series spatial data, based on the specified information of the sampled flow field data, which usually come from the experimental or numerical simulation results. As a result, fewer orthogonal basis expansions are used to approximate the description of the higher-order data, ultimately enabling the reconstruction and prediction of the flow field [25,26].

Considering the flow field characteristics of the hydrofoil, the incoming flow angle of attack and jet parameters are taken as state parameters, and the snapshot data obtained from the numerical simulation of the flow field are taken as sampling samples. As an example, with the pressure field $\{P(x)\} = \{P_{ij}(x) : 1 \le i \le M, 1 \le j \le N, x \in \mathbf{\Omega}\}$ under the variation of the incoming flow angle of attack α in a certain range, where M is the number of grid nodes, N is the number of appropriately selected samples, and $\mathbf{\Omega}$ is the flow field domain, the pressure field can be expressed as follows:

$$\{P_{ij}(x)\} = \begin{pmatrix} P_{11}(x) & P_{12}(x) & \cdots & P_{1N}(x) \\ P_{21}(x) & P_{22}(x) & \cdots & P_{2N}(x) \\ \vdots & \vdots & \vdots & \vdots \\ P_{M1}(x) & P_{M2}(x) & \cdots & P_{MN}(x) \end{pmatrix} \tag{5}$$

The average of N sets of pressure field snapshot data is denoted as follows:

$$\left\{\overline{P_i(x)}\right\} = \frac{1}{N}\sum_{j=1}^{N} P_{ij}(x), 1 \le i \le M \tag{6}$$

The pulsation value of the pressure field can be expressed as follows:

$$\{P_{ij}'(x)\} = P_{ij}(x) - \overline{P_i(x)}, 1 \le i \le M, 1 \le j \le N \tag{7}$$

The key to the POD method is to construct a set of optimal standard orthogonal basis functions $\varphi(x)$ that minimize the error value between the sampled samples and the constructed term in the least-squares sense, so that the projection of the basis functions $\varphi(x)$ onto the sampled samples achieves the maximum value,

$$\begin{cases} \max < \frac{1}{N}\sum_{j=1}^{N}\left|{P_{ij}}'(x), \varphi(x)\right|^2 \\ (\varphi(x), \varphi(x)) = \|\varphi(x)\|^2 = 1 \end{cases} \tag{8}$$

$(\varphi(x), \varphi(x))$ is the inner product and $\|\varphi(x)\|^2$ is the norm over the domain $\mathbf{\Omega}$. $\varphi(x)$ is a set of standard orthogonal bases of the vector set $\left\{{P_{ij}}'(x)\right\}$, then

$$\varphi(x) = \sum_{j=1}^{N} a_i {P_{ij}}'(x) \tag{9}$$

The maximum problem of the above equation can be solved by defining a kernel function and an operator between this kernel function and the desired basis, where the kernel function W and the operator R can be defined as follows:

$$W(x, x') = \left({P_{ij}}'(x), {P_{ij}}'(x')\right) \tag{10}$$

$$R\varphi(x) = \int_{\mathbf{\Omega}} W(x, x')\varphi(x')\mathrm{d}x' \tag{11}$$

Suppose the kernel function in the above is defined as follows:

$$W(x, x') = \frac{1}{N}\sum_{j=1}^{N} {P_{ij}}'(x){P_{ij}}'(x') \tag{12}$$

Bring this into Equation (11) and make an inner product of $\varphi(x)$ and $R\varphi(x)$:

$$\begin{aligned} &(\varphi(x), R\varphi(x)) \\ &= \int_{\mathbf{\Omega}} R\varphi(x)\varphi(x)\mathrm{d}x \\ &= \int_{\mathbf{\Omega}}\int_{\mathbf{\Omega}} W(x, x')\varphi(x')\mathrm{d}x'\varphi(x)\mathrm{d}x \\ &= \frac{1}{N}\sum_{j=1}^{N}\int_{\mathbf{\Omega}}\int_{\mathbf{\Omega}} {P_{ij}}'(x'){P_{ij}}'(x)\varphi(x')\mathrm{d}x'\varphi(x)\mathrm{d}x \\ &= \frac{1}{N}\sum_{j=1}^{N}\left|\left({P_{ij}}'(x), \varphi(x)\right)\right|^2 \end{aligned} \tag{13}$$

R is a non-negative symmetric operator. From Equation (12), we can see that the problem of finding the maximum value of Equation (8) is equivalent to the problem of finding the maximum eigenvalue of the operator R:

$$R\varphi(x) = \lambda\varphi(x), \|\varphi(x)\|^2 = 1 \tag{14}$$

Substituting Equations (9), (11) and (12) into Equation (14), we obtain

$$\sum_{j=1}^{N}\left[\sum_{k=1}^{N}\left(\frac{1}{N}\int_{\mathbf{\Omega}} {P_{ij}}'(x'){P_{ik}}'(x')\mathrm{d}x'\right)a_k\right]{P_{ij}}'(x) = \sum_{j=1}^{N}\lambda a_j {P_{ij}}'(x) \tag{15}$$

where ${P_{ij}}'(x)$ is a set of linearly independent pressure fields, which can be simplified to the following:

$$\mathbf{C}_{jk}A^l = \lambda A^l \tag{16}$$

The autocorrelation matrix is $C_{jk} = \frac{1}{N}\int_{\Omega} P_{ij}'(x)P_{ik}'(x)\mathrm{d}x$, and the eigenvector $A^l = \left[a_1^l, a_2^l, \cdots, a_N^l\right]^{\mathrm{T}}$. The matrix C_{jk} is a non-negative Hermitian matrix, usually of low order, so the Jacobi method or singular value decomposition (SVD) can be chosen to solve the eigenvalues and eigenvectors of the matrix.

In this paper, the SVD method is used to solve Equation (16) to obtain the matrix C_{jk} corresponding to the eigenvectors A^l, whose eigenvalues are ordered from smallest to largest as $\lambda_1 \geq \lambda_2 \geq \cdots \geq \lambda_l > 0$, and the standard orthogonal basis function (POD basis) can be obtained as follows:

$$\varphi_l(x) = \sum_{j=1}^{N} a_j^l P_{ij}'(x) \tag{17}$$

Any flow field in the sampled flow field can be projected onto the standard orthogonal basis functions $\varphi(x)$ to obtain the corresponding modal coefficients b_j^l, and the reconstructed flow field can be expressed as the following:

$$P_{POD}^l(x) = \sum_{l=1}^{N} b_j^l \varphi_l(x) \tag{18}$$

With the dimensionality reduction property of the POD method, after solving for the eigenvalues obtained, a suitable truncation order d (modal order) can be selected for dimensionality reduction, where $d << N$, where the magnitude of the eigenvalue represents its ability to capture the generalized flow field data E in the flow field:

$$E = \int \left\langle P_i'(x), P_i'(x) \right\rangle \mathrm{d}x = \int W_{ii}(x,x)\mathrm{d}x = \sum_n \lambda_n \tag{19}$$

The flow field is reconstructed by determining the order and modal coefficients corresponding to the modes using the POD method analysis approach. The modal coefficients are determined using an interpolated solution, and an efficient approximation to the original data space is achieved by small-scale computations of the modal orders and corresponding coefficients. This reduces the computational effort required for flow field simulation. The original sampled flow field is reconstructed with a low-order POD-ROM, and the reconstructed flow field can be expressed as the following:

$$P_{POD}^l(x) = \sum_{l=1}^{d} b_j^l \varphi_l(x) \tag{20}$$

3. Discussion and Analysis of Results

3.1. Flow Field Information Sampling

3.1.1. Flow Field without AFC

Typically, a BWB-UG glides at a speed of about 1Kn$(0.514\ \mathrm{m/s})$ with a small angle of attack. Therefore, in this paper, the numerical simulation is carried out for the base flow field with the inlet velocity $V_{inlet} = 0.514\ \mathrm{m/s}$ and the angle of attack α is set to $0^\circ \sim 12^\circ$ (with an interval of 0.6°). After the calculation, the pressure distributions of the hydrofoil surfaces under 21 operating conditions were used as sampling data to establish the reduced-order model, as shown in Figure 5.

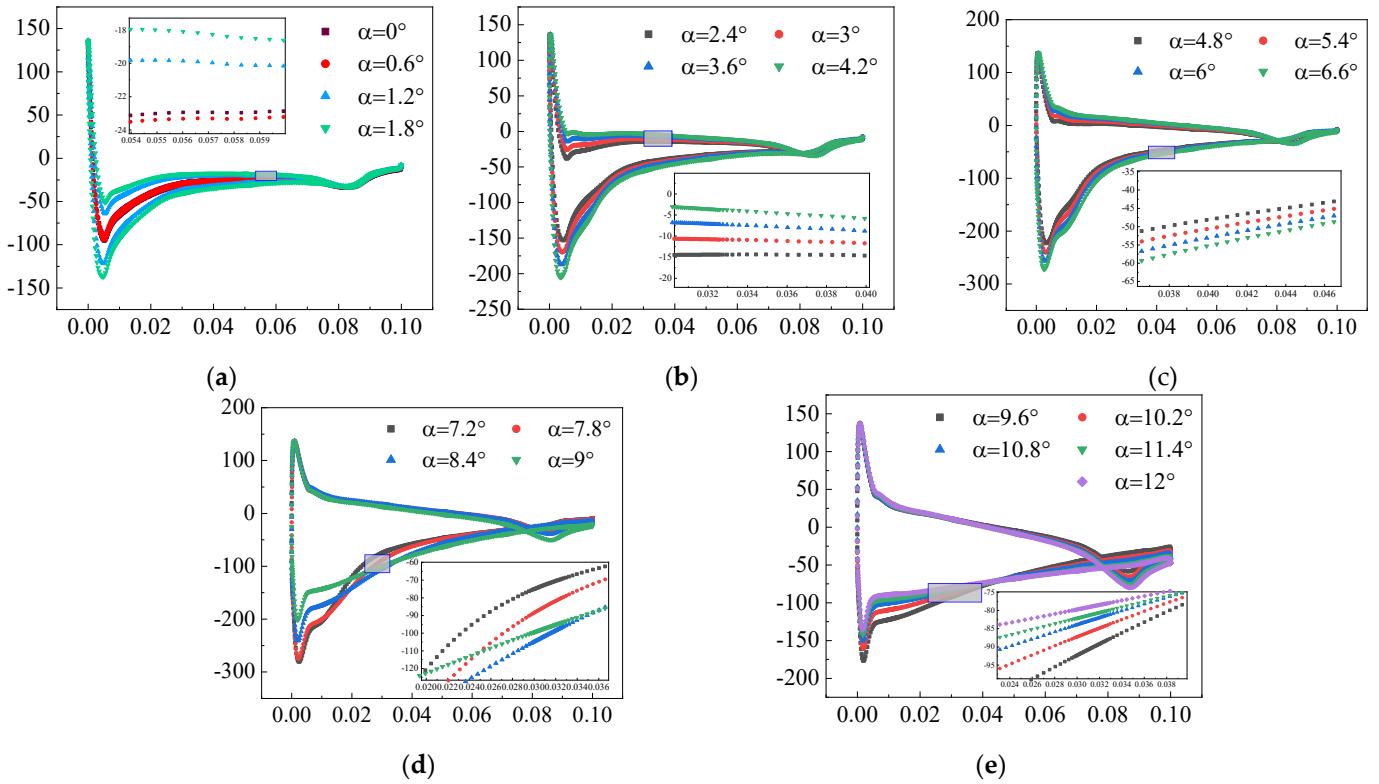

Figure 5. Surface pressure distribution of hydrofoil at different angles of attack in the base state; (**a**) $\alpha = 0°$~$1.8°$; (**b**) $\alpha = 2.4°$~$4.2°$; (**c**) $\alpha = 4.8°$~$6.6°$; (**d**) $\alpha = 7.2°$~$9.0°$; (**e**) $\alpha = 9.6°$~$12.0°$.

3.1.2. Constant Suction Control Flow Field

Firstly, the ROM of the constant suction AFC flow field in the hydrofoil is carried out, and the influence of suction velocity and suction angle on the control effect of the hydrofoil at different angles of attack is considered based on the CFD simulation. The magnitude of velocity is expressed by the suction velocity coefficient, $R_{suction} = V_{suction}/V_{inlet}$, with a range of values from 0.2 to 1.0 with an interval of 0.2. The suction deflection angle $\theta_{suction} = 30° \sim 150°$ at $30°$ intervals. The hydrofoil inlet velocity $V_{inlet} = 0.514$ m/s and the angle of attack α varied from $0°$ to $12°$ with an interval of $2°$. The cross-combined sampling method is used to calculate the flow field. When the angle of attack and suction velocity coefficient are changed, the suction deflection angle is set to a fixed value of $\theta_{suction} = 90°$, and when the angle of attack and suction deflection are changed, the suction velocity coefficient is a fixed value of $R_{suction} = 1.0$. Each combination corresponds to 35 groups of calculation conditions, and the hydrofoil surface pressure distribution under each condition is used as the sampling data to establish the reduced-order model of the constant suction active flow control flow field, and the specific condition adjustment is shown in Figure 6. With $\theta_{\text{suction}} = 90°$, the surface pressure distribution of the hydrofoil at different suction velocities and angles of attack is shown in Figure 7.

3.1.3. Constant Jet Control Flow Field

Secondly, the ROM of the constant jet AFC flow field in the hydrofoil is carried out. The effect of jet velocity and jet angle on the control effect of the hydrofoil at different angles of attack is considered. The magnitude of the velocity is expressed by the jet velocity coefficient $R_{jet} = V_{jet}/V_{inlet}$, which takes values from 0.2 to 1.0 at 0.2 intervals. The jet deflection angle $\theta_{jet} = 30° \sim 150°$ at $30°$ intervals. The hydrofoil inlet velocity is $V_{inlet} = 0.514$ m/s and the angle of attack α varied from $0°$ to $12°$ at $2°$ intervals. Similar to Section 3.1.2, when the angle of attack and the jet velocity coefficient are changed, the jet deflection angle is set to a fixed value of $\theta_{jet} = 90°$. Each combination corresponds

to 35 sets of computational conditions, and the hydrofoil surface pressure distribution is used as the sampling data for building a ROM of the jet-controlled flow field. With $\theta_{\text{jet}} = 90°$, surface pressure distributions of the hydrofoil at different constant jet velocities and different angles of attack are shown in Figure 8.

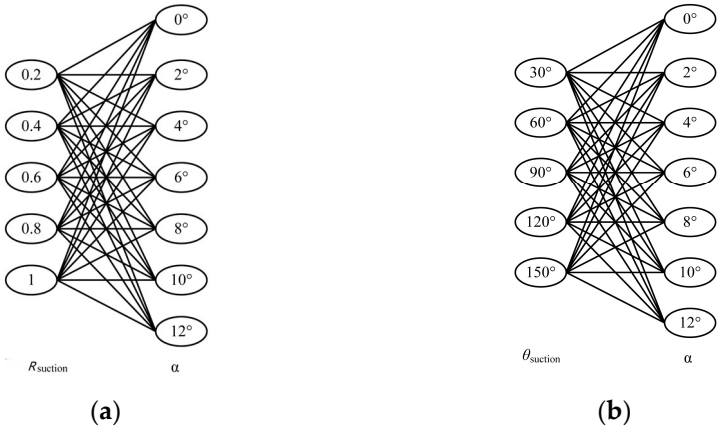

(**a**) (**b**)

Figure 6. Hydrofoil flow field conditions with different variable combinations for suction flow control. (**a**) Suction velocity coefficient + angle of attack of incoming flow; (**b**) Suction flow deflection angle + incoming flow angle of attack.

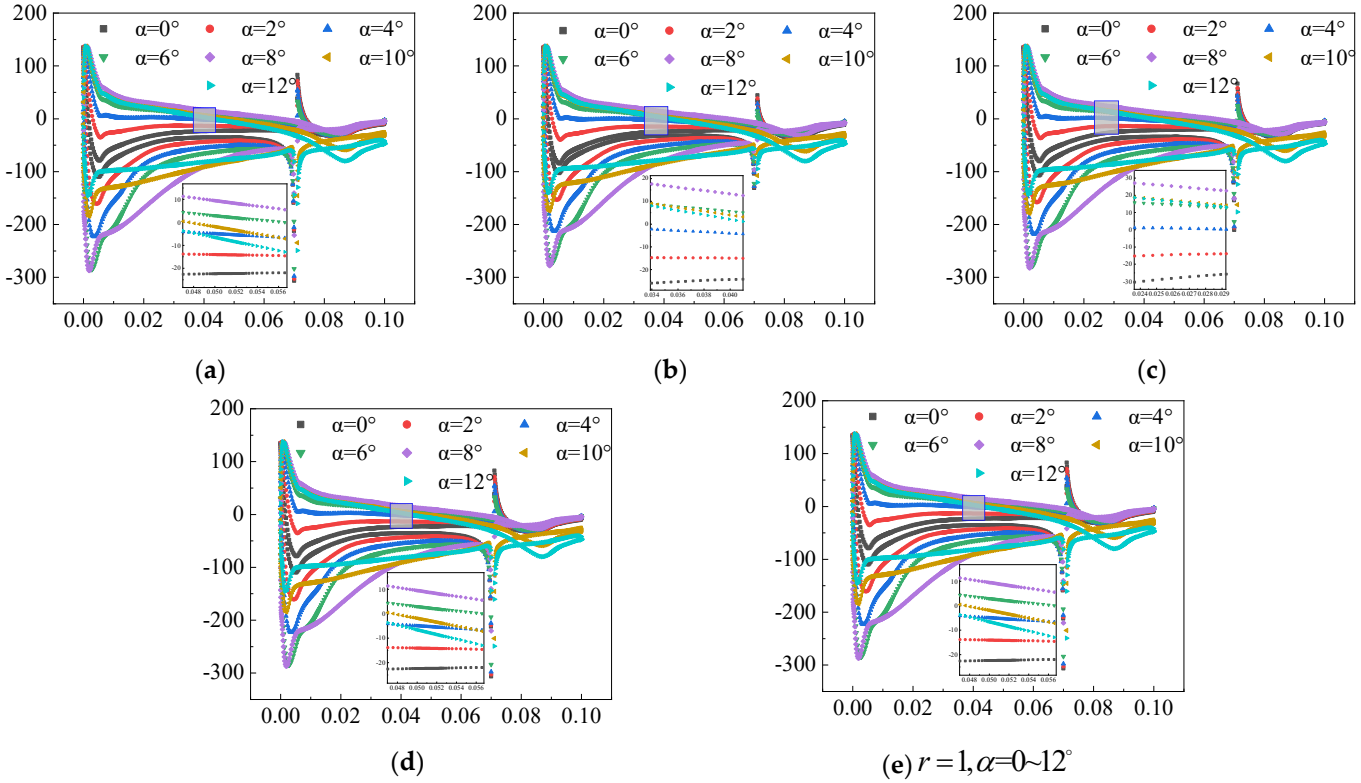

(**a**) (**b**) (**c**)

(**d**) (**e**) $r = 1, \alpha = 0 \sim 12°$

Figure 7. Surface pressure distribution of the hydrofoil at different suction velocities and angles of attack; (**a**) $R_{suction} = 0.2, \alpha = 0 \sim 12°$; (**b**) $R_{suction} = 0.4, \alpha = 0 \sim 12°$; (**c**) $R_{suction} = 0.6, \alpha = 0 \sim 12°$; (**d**) $R_{suction} = 0.8, \alpha = 0 \sim 12°$; (**e**) $R_{suction} = 1, \alpha = 0 \sim 12°$.

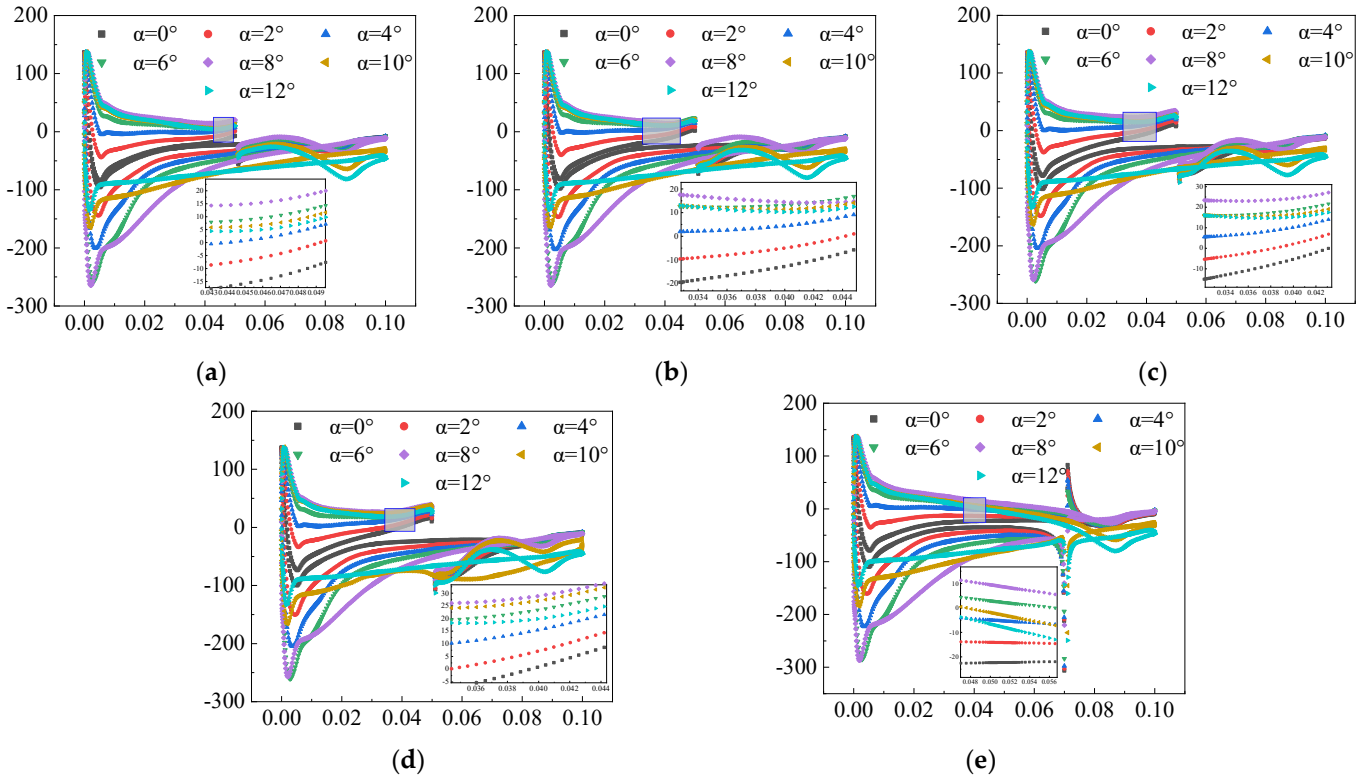

Figure 8. Surface pressure distribution of the hydrofoil at different constant jet velocities and different angles of attack; (**a**) $R_{jet} = 0.2, \alpha = 0 \sim 12°$; (**b**) $R_{jet} = 0.4, \alpha = 0 \sim 12°$; (**c**) $R_{jet} = 0.6, \alpha = 0 \sim 12°$; (**d**) $R_{jet} = 0.8, \alpha = 0 \sim 12°$; (**e**) $R_{jet} = 1, \alpha = 0 \sim 12°$.

3.2. Reconstruction of Flow Field Based on the POD Method

Based on the POD method, the modes are classified according to the difference in generalized energy levels based on the distribution characteristics of the eigenvalues of the flow field in the hydrofoil, and the order with a generalized energy share greater than 99% is taken as the truncation order d. The generated hydrofoil flow field data are subjected to the POD method, and the fundamental mode of the flow field and the corresponding eigenvalues can be obtained. The ratio of the sum of the eigenvalues corresponding to the first d-order fundamental modes to the sum of all eigenvalues is defined as the generalized energy share of the first d-order fundamental modes, which features characterize the amount of flow field information contained in the first d-order dominating modes. Mean relative error (MRE) is used as a measure of the accuracy of the reconstructed flow field data, and the MRE of the hydrofoil surface pressure field can be expressed as the following:

$$\varepsilon_P = \frac{1}{M}\sum_{m=1}^{M}\left(\left|\frac{P_{POD}^{(m)} - P_{CFD}^{(m)}}{P_{CFD}^{(m)}}\right| \times 100\%\right) \tag{21}$$

where M is the number of mesh nodes, $P_{POD}^{(m)}$ denotes the pressure value at the m-th grid node obtained from the reconstruction, and $P_{CFD}^{(m)}$ denotes the pressure value at the m-th grid node based on the CFD numerical simulation.

3.2.1. Flow Field without AFC

Based on the hydrofoil surface pressure data from the flow field without AFC, the incident angle of attack α is varied from $0° \sim 12°$ at 0.6° intervals, forming a sample size of $N = 21$, and the number of hydrofoil surface mesh nodes in each set of conditions is $M = 728$. The pressure distribution data at the mesh nodes on the surface of the 21 hydrofoils are selected as snapshot data, and the "pulsation amount" is used as a sample

to construct an $M \times N$ sample matrix. The eigenvalues and eigenvectors of this matrix are solved, and the distribution of the eigenvalues is shown in Figure 9. The magnitude of the captured generalized energy is given in Table 2, where the generalized energy equal to 99% corresponds to the truncation order $d = 3$. Therefore, the truncation order 3 is used as the modal order for the ROM of the pressure distribution on the hydrofoil surface.

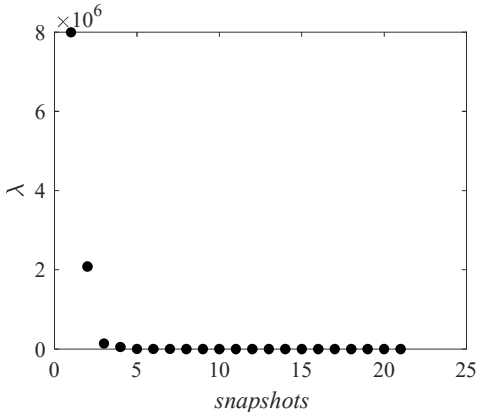

Figure 9. Distribution of eigenvalues of the base flow field.

Table 2. Comparison of the generalized energy captured cumulatively by the main eigenvalues of the base flow field.

Ordinal	Eigenvalue	Cumulative Captured Energy (%)
1	7.99×10^6	77.82
2	2.08×10^6	98.09
3	1.40×10^5	99.45

On this basis, the d-order POD basis is solved for the basal flow field in the hydrofoil after downscaling.

$$\varphi_{base}(x) = \sum_{j=1}^{3} a_j^l P_{ij}{}'(x) \tag{22}$$

where α_j^l is the coefficient obtained by solving for the autocorrelation matrix.

Based on the POD method, the corresponding modal coefficients b_j^l can be obtained by projecting any flow field in the sampled flow field onto the POD method to realize the reconstruction of the flow field.

$$P_{POD}^l(x) = \sum_{l=1}^{N} b_j^l \varphi_{base}(x) \tag{23}$$

Comparing the hydrofoil surface pressure distribution obtained from the POD step-down reconstruction with the CFD calculation data, it can be seen that the data are very similar, as shown in Figure 10. Comparing the average relative error under each working condition, it can be seen that when the hydrofoil is in the state of a small angle of attack $\alpha \leq 4.2^\circ$, the average relative error ε_P is smaller, less than 2%; it increases and shows a fluctuating change as α increases, and the maximum value is still less than 5%, as shown in Figure 11. The reason for this is that at high angles of attack, the separation zone near the trailing edge of the upper hydrofoil surface increases significantly, which changes the generalized energy distribution of the flow modes of the flow field and affects the surface pressure distribution, forming a localized low-pressure zone in the region of the trailing edge, with a significant change in the pressure gradient on the upper surface.

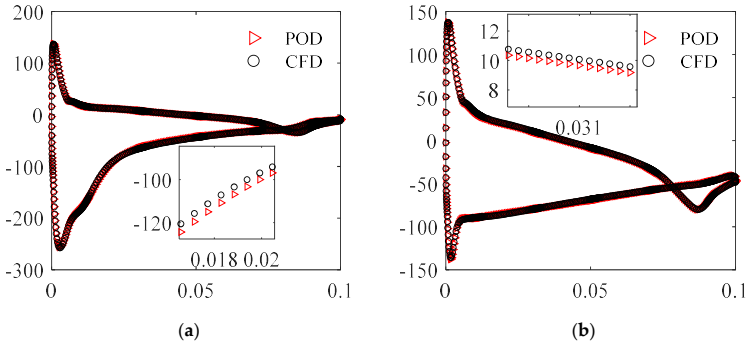

Figure 10. Comparison of hydrofoil surface pressure under base flow field; (**a**) α = 6°; (**b**) α = 12°.

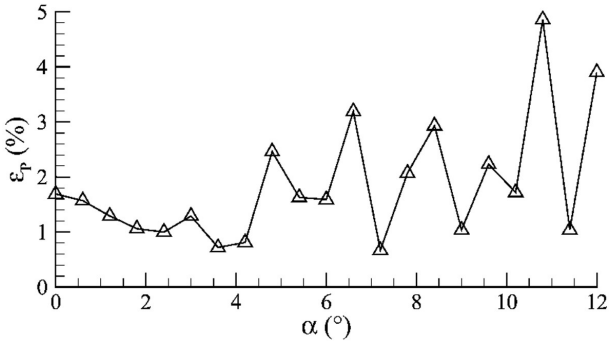

Figure 11. Variation in the mean relative error of hydrofoil surface pressure at different incoming flow angles of attack.

3.2.2. Constant Suction Control Flow Field

For the constant suction AFC field, the suction deflection angle and suction velocity are cross-combined with the angle of attack of the incoming flow, respectively, to establish a ROM of the AFC field. The hydrofoil surface pressure distribution is used with the sampling data with the number of grid nodes being $M = 719$. The suction deflection angle is $\theta_{suction} = 30° \sim 150°$ at 30° intervals, the angle of attack α is $0° \sim 12°$ at 2° intervals, and the suction velocity coefficient $R_{suction} = 1.0$ to form $N = 35$ sets of sampling conditions. The amount of pressure pulsation on the hydrofoil surface under each condition is used as the snapshot data to form a sampling matrix of $M \times N$. The eigenvalues and eigenvectors of this matrix are solved, and the distribution of the eigenvalues is shown in Figure 12. The magnitude of the captured energy is given in Table 3, where the energy equal to 99% corresponds to the truncation order $d = 11$. Therefore, $d = 11$ is used as the modal order for the ROM of the surface pressure distribution in the steady-state suction-controlled hydrofoil flow field.

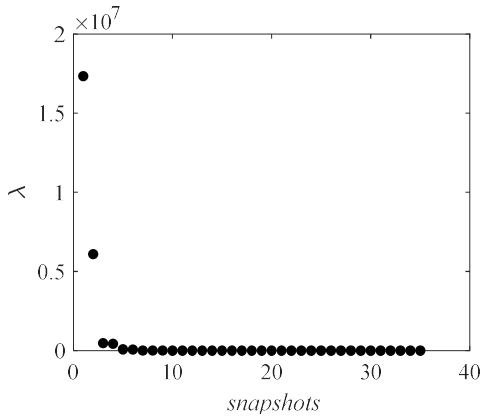

Figure 12. Distribution of the eigenvalues of the control flow field at different suction bias angles.

Table 3. Cumulative energy captured by the main eigenvalues of the flow field at different suction angle controls.

Ordinal	Eigenvalue	Cumulative Captured Energy (%)
1	1.73×10^7	70.73
2	6.09×10^6	95.58
3	4.76×10^5	97.52
...	...	...
11	8.84×10^2	99.99

Comparing the POD method with the CFD-calculated flow field data, it can be seen that the hydrofoil surface pressure distribution data are very similar in both cases, as shown in Figure 13. The average relative error ε_P of the hydrofoil surface pressure is less than 2% in most of the operating conditions, as shown in Figure 14.

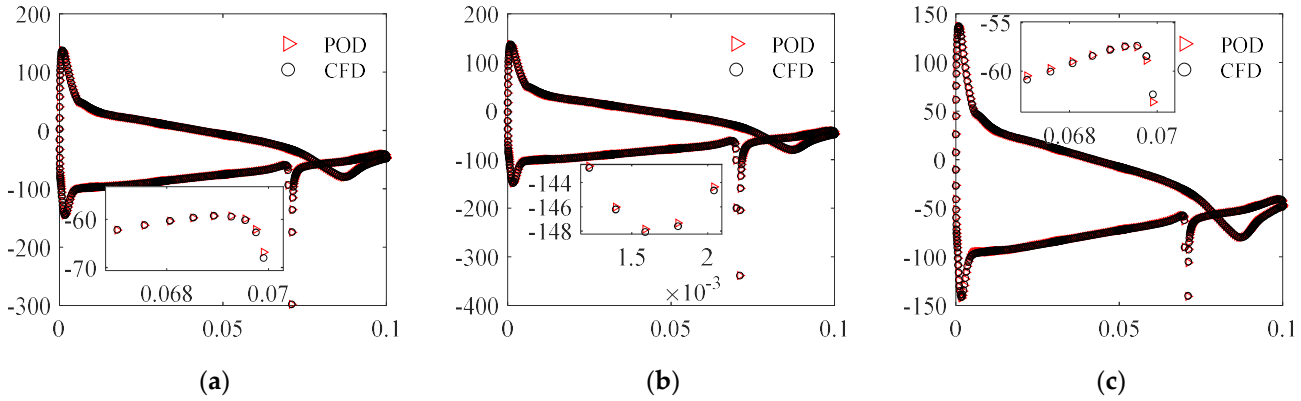

Figure 13. Comparisons of surface pressures of hydrofoil with different suction deflection angles at an angle of attack of 12°. (**a**) α = 12°, θ_{suction} = 30°; (**b**) α = 12°, θ_{suction} = 90°; (**c**) α = 12°, θ_{suction} = 150°.

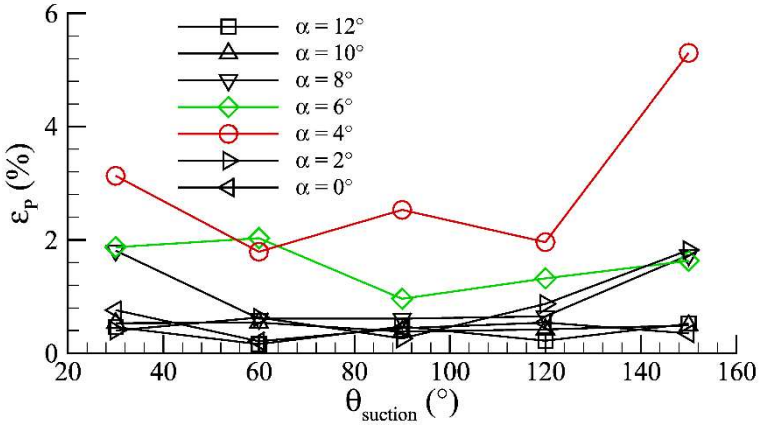

Figure 14. Variation in the mean relative error of surface pressure of suction-controlled hydrofoil at different angles of attack.

Subsequently, the suction deflection angle $\theta_{suction} = 90°$, the suction velocity coefficient $R_{suction} = 0.2$ to 1.0 at 0.2 intervals, and the angle of attack $\alpha = 0°$ to 12° at 2° intervals were investigated to form $N = 35$ sets of sampling conditions. The distribution of the eigenvalues is shown in Figure 15. The magnitude of the captur ed energy is given in Table 4. Using the same approach, $d = 10$ can be obtained as the modal order for the ROM of the surface pressure distribution in the steady-state suction-controlled hydrofoil flow field.

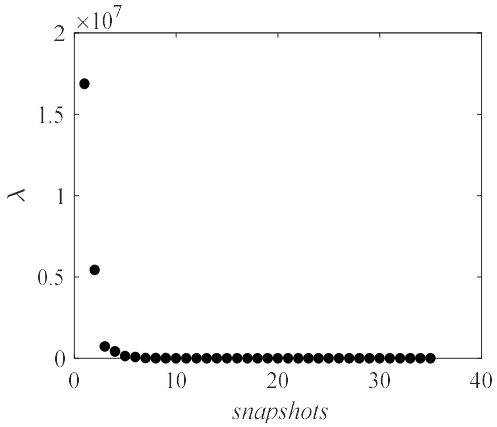

Figure 15. Distribution of the eigenvalues at different suction bias angles.

Table 4. Cumulative energy captured by the main eigenvalues of the flow field at different suction velocity coefficient controls.

Ordinal	Eigenvalue	Cumulative Captured Energy (%)
1	1.69×10^7	71.26
2	5.43×10^6	94.19
3	7.25×10^5	97.52
...	...	...
11	1.20×10^3	99.99

Similarly, when the flow field reconstructed by the POD method is compared with the flow field data calculated by CFD, it can be seen that the data of the hydrofoil surface pressure distribution are very similar in both cases, as shown in Figure 16. The average relative error ε_P of the hydrofoil surface pressure is less than 1% for most of the working conditions, as shown in Figure 17.

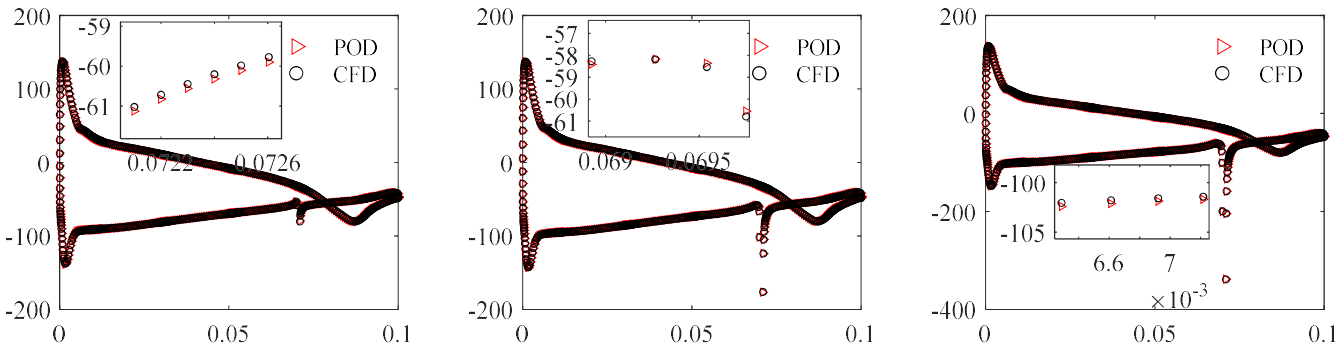

Figure 16. Comparison of surface pressures of hydrofoil with different suction deflection angles at 12° angle of attack. (**a**) α = 12°, R_{suction} = 0.2; (**b**) α = 12°, R_{suction} = 0.6; (**c**) α = 12°, R_{suction} = 1.0.

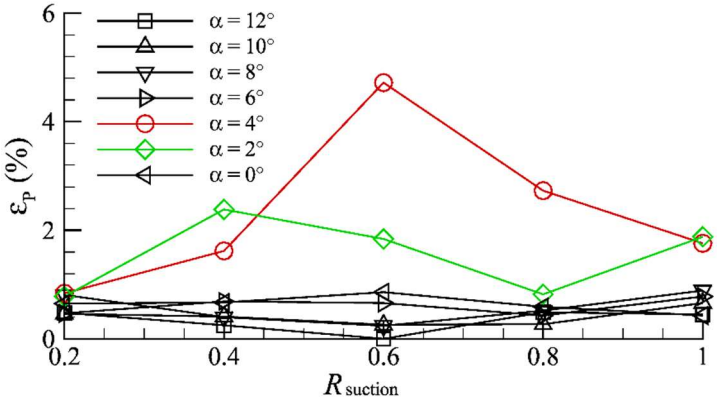

Figure 17. Variation in the mean relative error of surface pressure of suction-controlled hydrofoil at different suction velocity coefficients.

3.2.3. Constant Jet Control Flow Field

For the constant jet control flow field, the effects of the jet deflection angle and jet velocity coefficient on the control flow field are also analyzed. Using the same method, the truncation order d is determined based on the energy fraction of the flow field as well as the modes, which are 16 and 12, respectively, and the resulting eigenvalue distributions are shown in Figure 18. Comparing the POD downscaled reconstructed flow field with the CFD-calculated flow field data, it can be seen that the hydrofoil surface pressure distribution data are very similar in both cases, and the average relative error ε_P of the hydrofoil surface pressure is less than 1% for most of the working conditions, as shown in Figures 19 and 20.

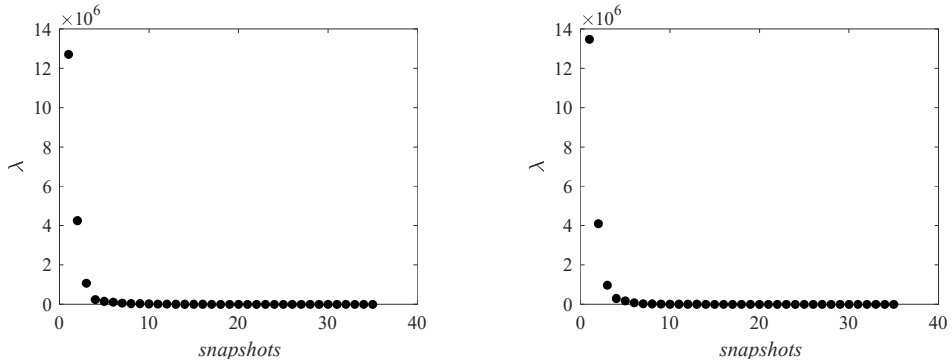

Figure 18. Distribution of eigenvalues of jet control flow field; (**a**) impact of jet deflection; (**b**) impact of jet velocity coefficients.

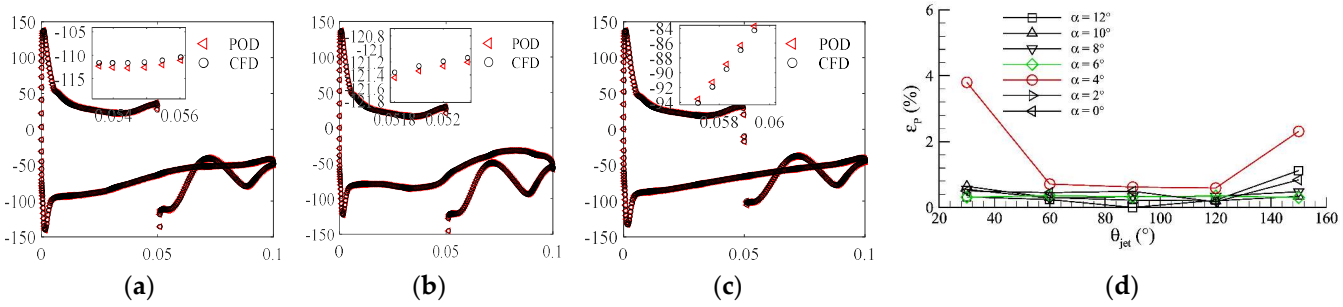

Figure 19. Comparison of surface pressure and error distribution of hydrofoil with different jet deflection angle control flow field. (**a**) α = 12°, θ_{jet} = 30°; (**b**) α = 12°, θ_{jet} = 90°; (**c**) α = 12°, θ_{jet} = 150°; (**d**) change in average relative error.

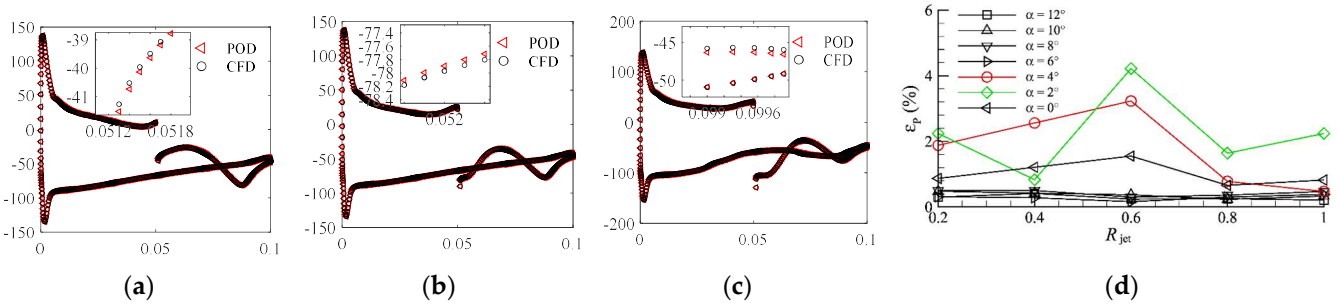

Figure 20. Comparison of surface pressure and error distribution of hydrofoil with different jet velocity coefficients to control the flow field. (**a**) α = 12°, R_{jet} = 0.2; (**b**) α = 12°, R_{jet} = 0.6; (**c**) α = 12°, R_{jet} = 1.0; (**d**) change in average relative error.

3.3. POD-ROM Flow Field Prediction

Based on the established POD-ROM, combined with the interpolated predictive modal coefficients, the predictive analysis of the flow field under any unknown state parameters is carried out and the results are compared with those of the CFD simulations. The working condition parameters, computation time, and error analysis are shown in Table 5, which shows that the average relative error of the hydrofoil surface pressure under the positional conditions predicted by the model is up to 6.9%, and its computation time is only in the order of 0.1 s, which is much smaller than that of the CFD simulation. The current errors are sufficient for engineering applications. The wall pressure distributions under different working conditions are shown in Figure 21. The results predicted by the ROM are close to the CFD simulation results, which can capture the main features of the flow field and verify the accuracy of the POD-ROM for predicting the flow field.

Table 5. Setting and error analysis of predicted flow field conditions.

Predicted Working Conditions	Working Condition Parameters	Computational Time(s)		ε_P
		POD	CFD	
Flow field without AFC	α = 7.5°	0.1	675	1.78
Suction-controlled flow field	α = 3°, θ = 75° Ratio = 1.0	0.1	1516	4.27
	α = 3°, Ratio = 0.5 θ = 90°	0.1	1770	3.42
Blowing controlled flow field	α = 3°, θ = 75° Ratio = 1.0,	0.1	575	6.90
	α = 3°, Ratio = 0.5 θ = 90°	0.1	445	1.59

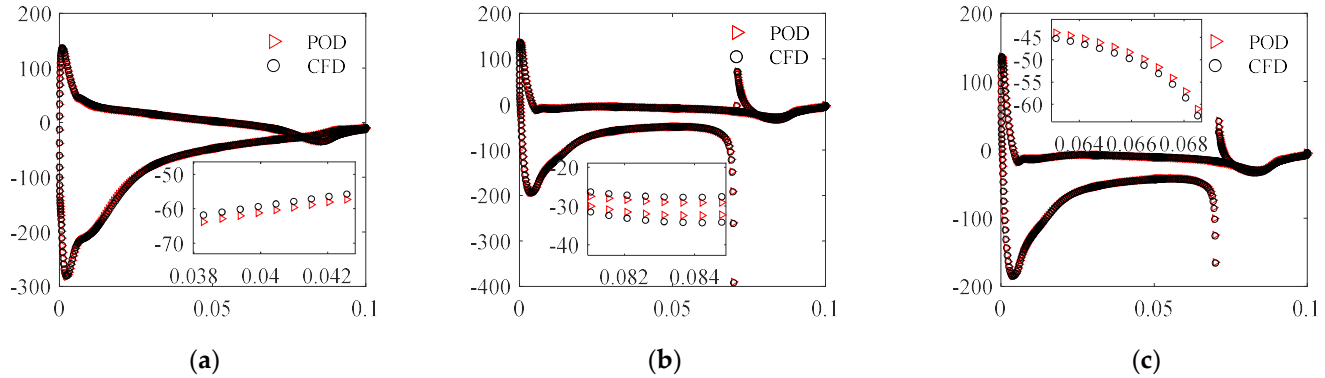

Figure 21. *Cont.*

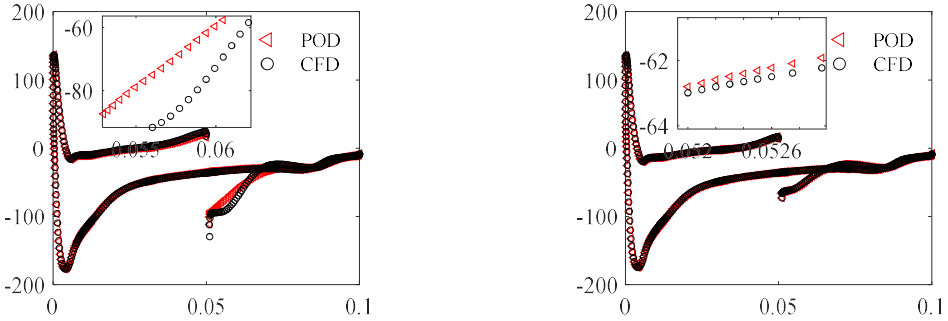

Figure 21. Comparison of pressure distribution in flow field predicted by POD-ROM. (**a**) Flow field without AFC α = 7.5°; (**b**) suction control α = 3°, θ = 75°, *Ratio* = 1.0; (**c**) suction control α = 3°, *Ratio* = 0.5, θ = 90°; (**d**) jet control α = 3°, θ = 75°, *Ratio* = 1.0; (**e**) jet control α = 3°, *Ratio* = 0.5, θ = 90°.

4. Conclusions

In this paper, based on the POD method, the ROM for the hydrofoil of the BWB-UG flow control with steady-stream suction and jets is investigated. The innovative POD method is used to solve the challenge of rapid flow field prediction in BWB-UG closed-loop active flow control. The established reduced-order model can effectively solve the timeliness problem of flow field calculation in closed-loop AFC, while the error of the model is sufficient to meet the needs of engineering applications. The main conclusions are as follows:

1. A POD-ROM prediction for the hydrofoil of the BWB-UG flow control with steady suction and blowing is successfully developed.

2. Compared to the CFD simulation, the computational time required to predict the target flow field using the established POD-ROM is only about 0.1 s, which is much less than the CFD simulation time.

3. The average relative error in predicting the surface pressure of the target using the established POD-ROM is less than 6.9% compared to CFD simulations. The established prediction model is valid.

The most difficult problem of closed-loop AFC is the timeliness of the flow field calculation, i.e., how to give relatively correct results in the shortest possible time. Therefore, in this paper, the investigation is carried out for a single variable. In future research, in-depth studies can be carried out for the reduced-order modeling containing multi-factors and high-dimensional data. The focus is on the nonlinear and strongly coupled relationship between multiple factors. This will provide more accurate guidance for closed-loop active flow control.

Author Contributions: Conceptualization, X.D. and H.W.; methodology, X.D. and Y.H.; software, H.W.; validation, X.D. and Y.H.; investigation, H.W.; resources, X.D. and Y.H.; data curation, H.W.; writing—original draft preparation, H.W.; writing—review and editing, H.W., X.D.; supervision, X.D. and Y.H.; project administration, X.D.; funding acquisition, X.D. All authors have read and agreed to the published version of the manuscript.

Funding: The author(s) disclosed receipt of the following financial support for the research, authorship, and publication of this article. This work is supported by the National Natural Science Foundation of China (No. U2341217).

Data Availability Statement: Data are contained within the article.

Conflicts of Interest: The authors declare no conflicts of interest.

References

1. Sun, C.Y.; Song, B.W.; Wang, P. Shape design and hydrodynamic characteristics analysis of the blended-wing-body underwater glider. *J. Ship Sci. Technol.* **2016**, *38*, 78–83. (In Chinese)
2. Du, X.X.; Zhang, L.Y. Numerical study on the steady suction active flow control of hydrofoil in the profile of the blended-wing-body underwater glider. *J. Northwestern Polytech. Univ.* **2021**, *39*, 801–809. (In Chinese) [CrossRef]
3. Zhang, X.L.; Du, X.X.; Ran, X.Z. Numerical Research on Active Flow Control with Synthetic Jet for Wing Section of Underwater Blended-wing-body Glider. *Shipbuild. China* **2022**, *63*, 95–106. (In Chinese)
4. Ren, F.; Wang, C.; Tang, H. Bluff body uses deep-reinforcement-learning trained active flow control to achieve hydrodynamic stealth. *Phys. Fluids* **2021**, *33*, 093602. [CrossRef]
5. Lu, T.; Hu, H.; Song, J.; Ren, F. Lattice Boltzmann modeling of backward-facing step flow controlled by a synthetic jet. *J. Hydrodyn.* **2023**, *35*, 757–769. [CrossRef]
6. Dong, H.; Geng, X.; Shi, Z.; Cheng, K.; Cui, Y.D.; Khoo, B.C. On evolution of flow structures induced by nanosecond pulse discharge inside a plasma synthetic jet actuator. *Jpn. J. Appl. Phys.* **2019**, *58*, 028002. [CrossRef]
7. Zhang, H.; Feng, Y. Review of Flow Control by Lorentz Force. *Aerodyn. Res. Exp.* **2023**, *1*, 20–29. (In Chinese)
8. Du, X.X.; Liu, X.; Song, D. Coupled physics analysis of blended-wing-body underwater glider equipped with electromagnetic active flow control. *Ocean. Eng.* **2023**, *278*, 114402. [CrossRef]
9. Zhang, L.; Gao, S.Q.; Zhao, J.X.; Tang, C.; Xie, H.L. Numerical simulation of influence of steady inhalation on aerodynamic performance of wind turbine. *Acta Energiae Solaris Sin.* **2018**, *39*, 2155–2162. (In Chinese)
10. Zhou, X.B.; Zhou, S.; Hou, A.P.; Zheng, X.Q. Numerical Investigation on Controlling Separated Cascade Flows by Using Jets. *Acta Aeronaut. Et Astronaut. Sinica* **2007**, *28S*, 7–13. (In Chinese)
11. Wang, B.X.; Yang, Z.G.; Zhu, H.; Li, Y.L. Drag Reducition by Active Control with Steady Blowing/Suction Methods. *J. Tongji Univ. (Nat. Sci.)* **2017**, *45*, 1383–1389. (In Chinese)
12. Du, X.; Liu, X.; Song, Y. Analysis of the Steady-Stream Active Flow Control for the Blended-Winged-Body Underwater Glider. *J. Mar. Sci. Eng.* **2023**, *11*, 1344. [CrossRef]
13. Chen, G.; Li, Y.M. Advances and prospects of the reduced-order for unsteady flow and its application. *Adv. Mech.* **2011**, *41*, 686–701.
14. Ren, F.; Gao, C.Q.; Tang, H. Machine learning for flow control: Applications and development trends. *Acta Aeronaut. Et Astronaut. Sin.* **2021**, *42*, 524686.
15. Ye, K.; Wu, J.; Ye, Z.Y.; Qu, Z. Analysis Circular Cylinder Flow Using Dynamic Mode and Proper Orthogonal Decomposition. *J. Northwestern Polytech. Univ.* **2017**, *35*, 599–607.
16. Lumley, J.L. Rational approach to relations between motions of differing scales in turbulent flows. *Phys. Fluids* **1967**, *10*, 1405–1408. [CrossRef]
17. Kidambi, K.B.; Mackunis, W.; Jayaprakash, A.K. Limit Cycle Oscillation Suppression Using a Closed-Loop Nonlinear Active Flow Control Technique. In Proceedings of the 59th IEEE Conference on Decision and Control (CDC), Jeju, Republic of Korea, 14–18 December 2020. [CrossRef]
18. Axia, W.; Yichen, M.; Wenjing, Y. The proper orthogonal decomposition method for the Navier-Stokes equations. *Acad. J. Xi'an Jiaotong Univ.* **2008**, *20*, 141–148.
19. Min, G.; Jiang, N. Data-driven identification and pressure fields prediction for parallel twin cylinders based on POD and DMD method. *Phys. Fluids* **2024**, *36*, 023614. [CrossRef]
20. Sun, F.J.; Zhu, D.H.; Zhang, D.M. Reduced-order model for fluid-structure coupled calculation of wind turbine blades. *J. Vib. Shock.* **2021**, *40*, 175–181+215. (In Chinese)
21. Wang, Y.G.; Li, Z.N.; Gong, B.; Li, Q.S. Reconstruction & prediction of wind pressure on heliostat. *Acta Aerodyn. Sin.* **2009**, *27*, 586–591. (In Chinese)
22. Kang, W.; Zhang, J.Z.; Li, K.L. Nonlinear Galerkin Method for Dimension Reduction Using Proper Orthogonal Decomposition. *J. Xi'an Jiaotong Univ.* **2011**, *45*, 58–62+67. (In Chinese)
23. Anderson, J.D.; Wendt, J. *Computational Fluid Dymanics*; McGraw-Hill Companies: New, York, NY, USA, 1995.
24. Menter, F.R. Two-equation eddy-viscosity turbulence models for engineering applications. *AIAA J.* **1994**, *32*, 1598–1605. [CrossRef]
25. Eiximeno, B.; Miró, A.; Rodríguez, I.; Lehmkuhl, O. Toward the Usage of Deep Learning Surrogate Models in Ground Vehicle Aerodynamics. *Mathematics* **2024**, *12*, 998. [CrossRef]
26. Lu, K.; Jin, Y.; Chen, Y.; Yang, Y.; Hou, L.; Zhang, Z.; Li, Z.; Fu, C. Review for order reduction based on proper orthogonal decomposition and outlooks of applications in mechanical systems. *Mech. Syst. Signal Process.* **2019**, *123*, 264–297. [CrossRef]